www.sciencemag.org/cgi/content/full/science.aad8022 /DC1

Supplementary Materials for

Nuclear magnetic resonance detection and spectroscopy of single proteins using quantum logic

I. Lovchinsky, A. O. Sushkov, E. Urbach, N. P. de Leon, S. Choi, K. De Greve, R. Evans, R. Gertner, E. Bersin, C. Müller, L. McGuinness, F. Jelezko, R. L. Walsworth, H. Park,* M. D. Lukin*

*Corresponding author. E-mail: lukin@physics.harvard.edu (M.D.L.); hongkun_park@harvard.edu (H.P.)

Published 4 February 2016 on *Science* First Release
DOI: 10.1126/science.aad8022

This PDF file includes:

Materials and Methods
Supplementary Text
Figs. S1 to S10
Table S1
Full Reference List

Materials and Methods

Chemical Attachment of Ubiquitin Proteins

Ubiquitin proteins (human, recombinant) labelled with ^{2}H and ^{13}C were purchased from Giotto Biotech (G03UBQ01). Ubiquitin proteins labelled with ^{13}C were purchased from Medical Isotopes, Inc (C3225). Unlabelled Ubiquitin was purchased from Sigma-Aldrich (709417). The reagents 1-ethyl-3-(-3-dimethylaminopropyl) carbodiimide hydrochloride (EDC), N-hydroxysuccinimide (NHS) and ethylenediamine were purchased from Sigma-Aldrich (E6383, 130672 and E26266, respectively).

We use carbodiimide crosslinker chemistry to attach ubiquitin proteins to the diamond surface. This procedure is designed so that any carboxylic acids terminating the diamond are conjugated to the linker molecule ethylenediamine, which is subsequently attached to the C-terminus of the protein. Conjugation of primary amines with carboxylic acids is achieved by crosslinking with the carbodiimide compound 1-ethyl-3-(-3-dimethylaminopropyl) carbodiimide hydrochloride (EDC). N-hydroxysuccinimide (NHS) is included in the reaction mixture to improve coupling efficiency.

Detector Sensitivity and Spectral Resolution

The modified XY8-k sequence leads to a NMR signal of the form

$$S(\tau) = \frac{1}{2}\Big(1 - \langle \cos\phi \rangle \Big), \tag{1}$$

where $\phi = 2\pi\gamma_e \int_{-\infty}^{\infty} dt f(t) B(t)$ is the total accumulated phase at the end of the sequence and the average is taken over many realizations of the experiment. Here $\hbar$ is the reduced Planck constant, $B(t)$ is the total magnetic field the NV center experiences over the course of the sequence and $f(t)$ is a series of step functions ranging between -1 and 1 that

describes the periodic π-phase rotations and free evolution intervals. If $B(t)$ is assumed to be normally-distributed with zero mean, the signal can be written as

$$S(\tau) = \frac{1}{2}\Big(1 - e^{-\langle\phi^2\rangle/2}\Big). \tag{2}$$

The mean phase variance $\langle\phi^2\rangle$ is given by the expression (*31, 32*)

$$\langle\phi^2\rangle = \frac{\gamma_e^2}{\pi}\int_{-\infty}^{\infty} d\omega \frac{S_B(\omega)F(\omega\tau)}{\omega^2}, \tag{3}$$

where $S_B(\omega) = \int_{-\infty}^{\infty} dt e^{i\omega t}\langle B(t)B(0)\rangle$ is the double-sided magnetic spectral density and $F(\omega\tau) = \frac{\omega^2}{2}|\tilde{f}(\omega)|^2$ is the detector filter function with $\tilde{f}(\omega) = \int dt e^{i\omega t} f(t)$ being the Fourier transform of the pulse sequence function. For the modified XY8-k sequence, the filter function is given by (*31*)

$$F(\omega\tau) = 2\sin^2\left(\frac{(k+1)\omega\tau}{2}\right)\tan^2\left(\frac{\omega\tau}{2}\right). \tag{4}$$

Here we have assumed that the durations of the spin rotation gates are much smaller than the free evolution intervals and can be neglected. Due to the dependence of $S(\tau)$ on the variance of the magnetic field, the NMR signal created by a single nuclear spin depends on the NV-spin separation r approximately as $1/r^6$. For an extended structure (e. g. an isotropic volume of protons, see below) the scaling could be significantly weaker. When the dimension of the structure is smaller than r, as is the case for the small protein considered in this work, the scaling is not appreciably different from that of a single nuclear spin.

In order to characterize the sensitivity we consider a monochromatic signal with random phase at frequency $2\pi\omega_0$, corresponding to the field spectrum

$$S_B(\omega) = \pi\langle B^2\rangle\,\delta(\omega - \omega_0) + \pi\langle B^2\rangle\,\delta(\omega + \omega_0). \tag{5}$$

The maximum of the NMR signal at this frequency occurs at $\tau_0 = \pi/\omega_0$ and is given by the expression

$$S(\tau_0) = \frac{\gamma_e^2}{\pi^2} \langle B^2 \rangle \tau_0^2 (k+1)^2 \tag{6}$$

Here we have made the small signal approximation $e^{-\langle \phi^2 \rangle/2} \approx 1 - \langle \phi^2 \rangle /2$. The maximum signal is achieved when the total sequence duration $\tau_0(k+1)$ is chosen to be approximately equal to the decoherence time T_2. Given a total averaging time T and a readout time T_R, $T/(T_2 + T_R)$ measurements can be performed, yielding the minimum detectable magnetic field variance δB^2, given by

$$\delta B^2 \approx \frac{\pi^2}{\gamma_e^2 T_2^2} \sqrt{\frac{T_2 + T_R}{T}}. \tag{7}$$

While this field variance is limited by spin projection noise, the dominant source of noise in our experiment is photon shot noise, which can be parameterized by the the NV center fluorescence readout fidelity (*5*)

$$\mathcal{F} = \left[1 + 2(\alpha_0 + \alpha_1)/(\alpha_0 - \alpha_1)^2 \right]^{-\frac{1}{2}}. \tag{8}$$

We define the sensitivity figure of merit of our nuclear spin sensing experiment as the number N of ^{1}H spins, situated on the diamond surface directly above the NV center, that can be detected with unity signal-to-noise ratio after $T = 1$ second of integration. The magnetic field variance of a single ^{1}H spin in this configuration is given by

$$B_p^2 \approx \frac{(\mu_0 \hbar \gamma_p)^2}{16\pi^2 d^6}, \tag{9}$$

where $\gamma_p = 2.68{\times}10^8$ s^{-1} T^{-1} is the proton gyromagnetic ratio, d is the NV center depth and μ_0 is the vacuum permeability. Thus, the sensitivity is given by

$$N \approx \frac{1}{\mathcal{F}} \frac{\delta B^2}{B_p^2}, \tag{10}$$

which yields Eq. 1 of the main text.

The spectral resolution Γ is given by the linewidth of the filter function and is fundamentally limited by the decoherence rate $1/T_2$. In the small signal approximation the FWHM linewidth W_F of the filter function in Eq. 5 is given by

$$W_F \approx \frac{0.886}{(k+1)\tau}. \tag{11}$$

NMR Sensing Area

For an NV center with depth d and a uniform, two-dimensional distribution of spins on the diamond surface, we determine that more than 70% of the NMR signal comes from a region of area πd^2 directly above the NV center. We define this region as the sensing area.

For typical NV depths ($d \sim 4$ nm) and the measured protein spacing ($\sim$21 nm), we expect to observe a ^{2}H NMR signal with amplitude of $> 1\%$ in approximately 10% of NV centers. Of these detection events, more then 90% are expected to be due to an individual protein. Here, detection of an individual protein is defined as the case in which more than 70% of the observed signal is created by a single protein.

Supplementary Text

1 Diamond Sample Processing

All experiments presented in this work were performed using two (100)-oriented, unpolished, electronic-grade diamond samples (henceforth referred to as samples A and B), consisting of a 50 μm ^{12}C-enriched (99.999% abundance) layer epitaxially-grown using plasma-enhanced chemical vapor deposition on a natural-abundance diamond substrate (Element Six). The concentrations of substitutional nitrogen and boron impurities were less than 5 parts per billion (ppb) and 1 ppb respectively. Sample A was implanted using a $^{15}N^+$ dosage of 10^9 cm^{-2} and an implantation energy of 2.0 keV. It was annealed in vacuum using the following procedure: (a) 6 hour ramp to 400°C, (b) 6 hours at 400°C, (c) 6 hour ramp to 800°C, (d) 8 hours at 800°C and (e) 6 hour ramp to room temperature. Sample B was implanted using a $^{15}N^+$ dosage of 10^{10} cm^{-2} and an implantation energy of 1.6 keV. It was annealed in vacuum using the following procedure: (a) 2 hours at 200°C, (b) 1 hour ramp to 800°C, (c) 1.5 hours at 800°C and (d) 2 hour ramp to room temperature.

After vacuum annealing, the samples were cleaned in a boiling 3-acid mixture (equal volumes of H_2SO_4, HNO_3, and $HClO_4$) for three hours. In order to reduce the decoherence rates of shallow NV centers, the samples were annealed in an oxygen environment (Tystar, Mini Tytan 4600) for 4 hours at 465°C. The oxygen anneal followed the following procedure: (a) ramp to 465°C for 2 hours, (b) anneal at 465°C for 4 hours, (e) ramp down to 250°C for 2 hours. The samples were placed in a Piranha solution (2:1 mixture of concentrated H_2SO_4 and 30% hydrogen peroxide) immediately before and after the anneal.

2 Optical Setup

We used a home-built, inverted confocal microscope to address individual NV centers. Here optical excitation was performed using a 532 nm diode-pumped solid-state (DPSS) laser (Information Unlimited, MLLIII532-200-1) modulated with an acousto-optic modulator (Isomet Corporation, 1250C-974) in a double-pass configuration. NV center fluorescence was separated from the reflected excitation beam using a dichroic beamsplitter, filtered using 532 nm notch and 633 nm long-pass filters and collected using a fiber-coupled single-photon counting module (PerkinElmer, SPCM-AQRH-14-FC). A Nikon Plan Fluor 100x oil immersion objective (NA = 1.3) was positioned under a microwave-frequency coplanar waveguide, used to hold the diamond sample. A layer of objective immersion oil (Micro Video Instruments, Inc, MVA22024) was placed between the waveguide and the sample to reduce aberrations and increase collection efficiency. Lateral steering of the laser beam was performed using a closed-loop scanning galvanometer (Thorlabs GVS012) while the vertical position of the focus was controlled with a with a piezoelectric stage (Physik Instrumente P-721 PIFOC). The acousto-optic modulator and the single-photon counting module were gated using TTL pulses produced by a 500 MHz PulseBlasterESR-PRO pulse generator from Spincore Technologies.

3 Coherent Control of Two-Qubit Register

3.1 Manipulation of Electronic Spin Qubit

We apply microwave-frequency (MW) drive fields using a coplanar waveguide fabricated on a silicate glass substrate (Ted-Pella, Inc, #260320). Here we use a Sharon Thermal Evaporator to deposit a three-layer metal structure consisting of a 50 nm titanium adhesion layer, 1000 nm of of copper and 300 nm of gold. The metal surface is then coated

with Shipley S1813 positive photoresist and a coplanar transmission line structure is generated using optical lithography (SUSS MicroTec MJB4). The resist is developed using Microposit MF CD-26 developer and the exposed metal is removed using Au etch and hydrofluoric acid (HF). The unexposed resist is removed with acetone and the finished waveguide is cleaned using Buffered Oxide Etch (7:1). In order to prevent the diamond sample from coming into direct contact with the metal, the waveguide is coated with a 20 nm film of aluminum oxide (Al_2O_3) using Atomic Layer Deposition (Cambridge NanoTech, S200).

We apply strong MW pulses at the carrier frequency $\frac{\gamma_e}{2\pi}B - \Delta$ in order to rotate the electronic spin irrespective of the ^{15}N spin state (Hadamard, Pauli-X and Pauli-Y gates). Here $\Delta = 2.87$ GHz is the NV center zero-field splitting, $\gamma_e = 1.76{\times}10^{11}$ s^{-1} T^{-1} is the electron gyromagnetic ratio and B is the magnitude of the external magnetic field applied along the NV symmetry axis. For all measurements presented in this work, strong MW pulses are 12-25 ns in duration. The MW signal is generated by a Stanford Research Systems SG384 signal generator where the built-in IQ modulation inputs are used to control the x and y quadrature amplitudes of the output signal. The MW pulses are gated by a dual-output Tektronix 3052C Arbitrary Function Generator (AFG), which is in turn triggered by TTL pulses. A second AFG controls the IQ modulation of the output signal.

We apply a weak MW π-pulse resonant with one of the ^{15}N hyperfine transitions to implement the C-NOT gate (henceforth referred to as C-NOT$_{e|n}$)

$$|0\downarrow\rangle \rightarrow |0\downarrow\rangle\,, |1\downarrow\rangle \rightarrow |1\downarrow\rangle\,, |0\uparrow\rangle \rightarrow |1\uparrow\rangle\,, |1\uparrow\rangle \rightarrow |0\uparrow\rangle\,, \tag{12}$$

where the electronic spin is flipped conditioned on the nuclear spin state. Here the carrier frequency of the tone is set to $\frac{\gamma_e}{2\pi}B - \Delta - A/2$, where $A \approx 3.05$ MHz is the hyperfine

coupling between the NV center electronic spin and the ^{15}N nuclear spin. The MW signal is synthesized using a Rhode&Schwarz SMC100A signal generator, frequency-doubled with a Mini-Circuits ZX90-2-36-S+ multiplier and power boosted with a Mini-Circuits ZHL-16W-43-S+ amplifier. Setting the duration of the π-pulse to $\sim$280 ns yields a frequency profile with a zero at the detuning that corresponds to the other ^{15}N hyperfine line, effectively applying a 2π-pulse to the off-resonant transition.

An external static magnetic field was applied using a permanent neodymium magnet on a goniometric stage (Edmund Optics, #66-532).

3.2 Modified XY8-k Sequence

We optically-polarize the NV center electronic spin into the state $|0\rangle$ and apply a Hadamard gate to create the superposition state $(|0\rangle + |1\rangle)/\sqrt{2}$. The spin then undergoes k periodic π-phase rotations separated by intervals of free evolution, after which a final Hadamard gate converts any accumulated phase into a measurable population difference. In contrast to the canonical XY8-k sequence, the $k+2$ spin rotations are implemented using a train of identically-spaced MW pulses where the amplitudes are controlled via IQ modulation. The phases of the π-pulses follow the pattern

$$[X]_1[Y]_2[X]_3[Y]_4[Y]_5[X]_6[Y]_7[X]_8 \cdots [X]_{k-2}[Y]_{k-1}[X]_k, \tag{13}$$

where $[X]$ and $[Y]$ correspond to Pauli-X and Pauli-Y gates, respectively. In order to cancel the DC component of the magnetic field noise spectrum we require an odd number of π-pulses. As an illustration, an XY8-11 sequence in this scheme would have the form

$$[X]_{\pi/2}[X]_\pi[Y]_\pi[X]_\pi[Y]_\pi[Y]_\pi[X]_\pi[Y]_\pi[X]_\pi[X]_\pi[Y]_\pi[X]_\pi[X]_{\pi/2}, \tag{14}$$

with each pulse separated by time interval τ.

3.3 Manipulation of Nuclear Spin Qubit

A radio-frequency (RF) drive field is delivered through a copper coil positioned above the diamond sample. We use a high-purity alumina rod as the inductor core in order to efficiently dissipate heat created by the high power RF pulses.

The RF tone at the carrier frequency $A - \frac{\gamma_N}{2\pi}B$, where γ_N is the ^{15}N gyromagnetic ratio, is used to implement the C-NOT gate (henceforth referred to as C-NOT$_{n|e}$)

$$|0\downarrow\rangle \rightarrow |0\downarrow\rangle, |0\uparrow\rangle \rightarrow |0\uparrow\rangle, |1\downarrow\rangle \rightarrow |1\uparrow\rangle, |1\uparrow\rangle \rightarrow |1\downarrow\rangle. \tag{15}$$

Here the signal is synthesized using a second Rhode&Schwarz SMC100A generator and amplified using a ENI A-500 RF amplifier. For all measurements presented in this work the RF pulses are 50-60 μs in duration.

3.4 SWAP Operation

A SWAP operation, which interchanges the nuclear and electronic spin states, is equivalent to the sequence C-NOT$_{e|n}$ − C-NOT$_{n|e}$ − C-NOT$_{e|n}$. For repetitive readout of the electronic spin populations, where the coherence of the final state is irrelevant, the last C-NOT$_{e|n}$ gate is not strictly necessary.

3.5 Quantum Logic-based Readout

The inefficiency of optical readout of NV centers is due to the fact that the optical excitation used for readout also re-polarizes the NV center spin before enough photons can be detected to accurately determine its state. In order to improve the readout fidelity, we utilize a two-qubit quantum register, consisting of an NV center electronic spin and its associated ^{15}N nuclear spin. Here, the nuclear and electronic qubits are coupled through the hyperfine interaction, resulting in the level structure shown in Fig. S1, where the $|0\rangle$

and $|1\rangle$ correspond to the $m_s = 0$ and $m_s = 1$ magnetic sublevels of the NV electronic spin, respectively, while the states $|\downarrow\rangle$ and $|\uparrow\rangle$ denote the eigenstates of the ^{15}N nuclear spin ancilla. As shown in Fig. 1b of the main text, by applying a SWAP quantum gate followed by an electronic repumping operation, an arbitrary electronic spin state $\alpha|0\rangle + \beta|1\rangle$ is stored in the ancilla qubit, resulting in the state $|0\rangle \otimes (\alpha|\downarrow\rangle + \beta|\uparrow\rangle)$, irrespective of the initial nuclear spin state. Subsequently, a controlled-NOT (C-NOT) gate, implemented using a weak MW pulse resonant with one of the ^{15}N hyperfine transitions (blue arrow in Fig. S1), creates the entangled state $\alpha|0\downarrow\rangle + \beta|1\uparrow\rangle$. An optical measurement (of duration 800 ns) then projects this state into either $|0\downarrow\rangle$ or $|1\uparrow\rangle$ and re-polarizes the electronic spin. The sequence of C-NOT and optical readout is then repeated with each additional cycle (of duration 1.1 μs) yielding more information about the initial spin populations.

In all measurements employing repetitive readout, the transition frequency of the $m_s = 0$ and $m_s = 1$ magnetic sublevels of the NV center is tuned as far as possible from the excited state level anti-crossing (*10*). This ensures that the effect of the depolarization of the ^{15}N nuclear spin mediated by hyperfine coupling in the excited state of the NV center is minimized.

In order to reduce the effect of spurious noise (e. g. slow drift of the ESR line), the repetitive readout sequence is repeated twice. The first run includes the magnetic signal acquisition while the second run includes instead a single strong MW pulse, used for normalization. For all NMR measurements presented in this work, where repetitive readout is utilized, we use 500 readout cycles.

4 NV Center Depth and Decoherence Rate Measurements

In this work the depths of NV centers are measured by immersing the sample into microscope objective immersion oil and detecting the amplitude of the ^{1}H NMR signal created at the NV center by the proximal proton spins. It can be shown (*18*) that for a (100)-oriented diamond surface, the magnetic field variance along the NV center axis created by the statistically-polarized ensemble of protons is given by the expression

$$\langle B^2 \rangle = \frac{5\rho\mu_0^2\mu_N^2 g_p^2}{1536\pi d^3}. \tag{16}$$

Here ρ is the proton density, μ_0 is the vacuum permeability, μ_N is the nuclear magneton, $g_p \approx 5.59$ is the proton g-factor and d is the NV center depth. We assume a Lorentzian field spectrum given by the expression

$$S_B(\omega) = \frac{\langle B^2 \rangle \gamma}{\gamma^2 + (\omega - \omega_0)^2} + \frac{\langle B^2 \rangle \gamma}{\gamma^2 + (\omega + \omega_0)^2}, \tag{17}$$

where γ is a spectral width that captures the dephasing and motional effects of the proton bath. We fit the measured ^{1}H NMR spectrum to the expressions given in Eq. 5 and Eq. 6 of Methods using the field spectrum from the expression above. The fitting parameters γ and d yield the coherence timescale of the proton bath and the depth of the NV center, respectively. A more complete treatment of this topic is provided in [32].

The decoherence rates of NV centers are estimated by sampling the amplitude of the magnetic field noise spectrum $S_B(\omega)$ at different frequencies. Here we sweep the free evolution interval τ between π-pulses in the XY8-k sequence. The data is fit to the expression (*11*)

$$D(\tau) = \frac{1}{2}\Big(1 - \exp\left[-(\Gamma\tau)^p\right]\Big), \tag{18}$$

where Γ is the NV center decoherence rate and p is a value ranging from 1-3. All NMR measurements presented in this work are processed by subtracting the observed NMR signal from D and dividing by $1 - 2D$ to reflect the reduced contrast created by NV decoherence. Here the levels of 0 and 1 correspond to the fluorescence rates of the $m_s = 1$ and $m_s = 0$ magnetic sublevels of the NV center, respectively.

5 Sensitivity of Nuclear Spin Sensing

As illustrated in Fig. S2a of the main text, the oxygen surface treatment combined with quantum logic-based readout yields shallow NV centers with sensitivities improved by more than a factor of 500 as compared to the same NV centers before surface treatment and using conventional readout. We note that although the increase in coherence times using oxygen annealing has been reproduced in multiple samples, the corresponding decrease in NV depth has only so far been observed in a single sample. In Fig. S2a we compare the sensitivity gain to a selection of previous work reported in the literature (*3, 11, 18, 33*). Only studies where the NV depths were measured directly (*32*), as opposed to estimated from ion implantation simulations, are considered. Here we do not consider reporter-based spin sensing (*4*): while this method yields single proton sensitivity, it does so at the cost of a much smaller sensing volume, due to the short coherence times of reporter spins on the diamond surface.

The error bars in Fig. S2a represent the mean values of the measured NV center sensitivities. The error bars correspond to 75% quantiles for cases when more than a single NV center was measured. We use a readout fidelity $\mathcal{F} = 0.2$ for the present case when quantum logic-based readout is used (as shown in Fig. 1c). A value of $\mathcal{F} = 0.03$, corresponding to a typical fluorescence rate of 100 kCts/s, a detection window of 250 ns and a fluorescence contrast of 35% between the $m_s = 0$ and the $m_s = \pm 1$ states of the

NV center, is assumed for all other cases. In all cases presented here, the coherence time was measured with an XY8-k pulse sequence with k between 64 and 448. In cases where the coherence time was measured using more than one value of k, we chose the maximum reported coherence time for the present analysis.

The sensitivity can be further improved through several proposed routes. Employing Hartmann-Hahn double resonance (HHDR), the NMR sequence acquisition time can be increased from T_2 to T_1^ρ, the longitudinal relaxation time in the rotating frame (*22*). As shown in Fig. S2b, we measure coherent spin locking times T_1^ρ up to $\sim$1 ms, more than a factor of 10 longer than T_2 with $\sim$100 π-pulses, which could translate to almost two orders of magnitude of additional increase in sensitivity. Furthermore, HHDR allows nuclear spins to be hyperpolarized, as demonstrated in [22]. This scheme yields a sensitivity figure-of-merit that is linearly, rather than quadratically, dependent on the nuclear magnetic moment (*5*), yielding a 10-fold improvement in detection sensitivity when the nuclear spin relaxation time T_1^n is longer than the signal acquisition time. If background protons can be removed from the diamond by deuterating the surface (*3*), ^{1}H spins can be used for indirect detection of nuclei with low magnetic moments (*24*). In the specific case ^{2}H or ^{13}C sensing demonstrated here, this proton-assisted scheme would yield a 16-fold increase in sensitivity.

6 Characterization of Protein Attachment

6.1 Surface Topography Characterization using AFM

An Asylum MFP-3D Atomic Force Microscope (AFM) is used to characterize the surface topography of our diamond samples. We operate the AFM in tapping mode using Olympus AC240TS probes (tip radius 9 $\pm$ 2 nm, resonance frequency $\sim$70 kHz). The samples are mounted onto glass microscope slides using nonconductive double-sided ad-

hesive discs. The microscope is calibrated using a 1.5 nm SiC step calibration sample (Ted Pella 629-90AFM).

After attaching ubiquitin proteins to the diamond surface, we characterize the resultant topographic features in AFM (Fig. 2c) by fitting a Gaussian surface to each feature. We define the height and radius of each feature (Fig. 2d) as the maximum and the half-width, half-maximum of the Gaussian surface, respectively. The zero of height corresponds to the diamond surface and was determined by fitting several well-resolved features in the four corners of the image where the baseline offset was left as a free parameter. To determine which features to include in the histograms, we smooth the raw image with a Gaussian filter with standard deviation of 1 pixel and define the peaks as all pixels with a higher value than its eight immediate neighbors. Features with height lower than the diamond surface, likely corresponding to spurious noise peaks, as well as edge features are neglected. Using four large (1 x 1 μm) AFM scans, corresponding to three different diamond samples and three instances of the chemical attachment procedure, we extract a mean spacing of 25.8 $\pm$ 0.4 nm for the observed topographic features.

Assuming a randomly distributed ensemble of proteins (an assumption validated by experiments described below), we expect a fraction to be unresolved due to the resolution limit imposed by the size of the AFM probe. Thus the mean spacing of observed spots, as extracted using the method described above, underestimates the number of proteins on the surface. Accounting for this effect, we extract a corrected mean protein spacing of 21.6 $\pm$ 0.4 nm.

The proteins can be removed from the diamond surface by repeating the cleaning procedure outlined in section 1, as shown in Fig. S3.

6.2 Protein Density Calibration using Cy3 Fluorophores

In order to independently calibrate the surface density of attached proteins, we conjugate Cy3 dye molecules to ubiquitin proteins using a commercial conjugation kit (Abcam ab188287) and attach the resulting complex to the diamond surface using the chemistry procedure described in Methods. The fluorophores are imaged using the confocal microscope setup described in section 2. Here, we use a 2 μW, 532 nm laser for excitation and detect the dye fluorescence using a 532 notch and a 633 shortpass filter. As shown in Fig. S4a, the surface yields uniform fluorescence and the dye can be readily photobleached using continuous laser excitation (Fig. S4b), where we observe the expected stretched exponential decay resulting from the range of photobleaching timescales of fluorophores located in different points within the Gaussian point spread function. The optical fluorescence spectrum of the surface (Fig. S4c) shows the characteristic double-peaked structure of the Cy3 dye spectrum with a maximum at $\sim$570 nm.

We extract the surface protein density in two independent ways. First, we dilute our Cy3+ubiquitin solution so that the resulting surface coverage yields well-resolved spots (Fig. S4d) and find that the spots fluoresce significantly more below 633 nm than above this wavelength, consistent with the Cy3 spectrum measured at high concentration. Fig. S4e shows a representative photobleaching timetrace of an individual spot. We image a large number of resolved spots and fit each one with a Gaussian surface function, extracting a mean fluorescence amplitude of 9.3 $\pm$ 1.1 kCts/s. Here, we acquire three consecutive images of the diamond surface. Only spots that appear in all three images and those that yield fits with amplitudes higher than one standard deviation above the background fluorescence level are chosen for analysis. The maximum fluorescence level of each spot is extracted from an average of the three images. Assuming that the observed spots are individual Cy3+ubiquitin complexes, the mean fluorescence at low concentration

allows us to extract a mean protein spacing at high concentration of 20.9 ± 1.4 nm, consistent with that measured in AFM. Here the error bar corresponds to the uncertainties in the mean fluorescence rate of individual Cy3+ubiquitin complexes as well as the mean surface fluorescence rate of Cy3+ubiquitin at high concentration (Fig. S4a).

As an independent verification, we attach to the diamond surface a dilute concentration of bare Cy3 dye molecules and observe their characteristic photobleaching behavior (Fig. S4f). From measurements of many such timetraces we extract a mean fluorescence rate of 1.5 ± 0.2 kCts/s. The performed conjugation chemistry described above is expected to attach a dye molecule to every exposed amine group with high probability. Assuming that all seven of the exposed Lysine residues in ubiquitin, as well as its N-terminus are conjugated with Cy3, we extract a mean protein spacing at high concentration of 23.8 ± 1.6 nm, again consistent with that measured in AFM. Here the error bar corresponds to the uncertainties in the mean fluorescence rate of individual Cy3 dye molecules as well as the mean surface fluorescence rate of Cy3+ubiquitin at high concentration (Fig. S4a).

7 NMR of ubiquitin proteins

7.1 NV-based ^{2}H and ^{13}C NMR of ubiquitin proteins

Fig. S5 shows ^{2}H and ^{13}C NMR spectra of ubiquitin proteins, enriched with deuterium and carbon-13, as measured on three NV centers (NV A, NV B and NV C, with corresponding depths of 2.9 ± 0.2 nm, 3.8 ± 0.1 nm and 3.8 ± 0.2 nm, respectively).

Fig. S6 (panels a,c and e) shows ^{13}C NMR spectra of ubiquitin proteins, enriched only with carbon-13, as measured on three NV centers (NV D, NV E and NV F with corresponding depths of 3.8 ± 0.4 nm, 6.5 ± 0.6 nm and 3.6 ± 0.5 nm, respectively). Panels b, d and f show the NMR spectra (in the ^{13}C spectral range) measured on the same three NV centers after the proteins have been removed from the surface. The

lineshapes for both the ^{2}H and ^{13}C NMR spectra are approximated by gaussian functions and convolved with the detector filter function. The shaded green regions denote the spectral resolution.

Fig. S7 shows several examples of NMR spectra measured on NV centers where no proximal protein was detected. Panels a, c and e show ^{2}H NMR spectra measured on three NV centers (with depths of 4.7 $\pm$ 0.3 nm, 4.8 $\pm$ 0.4 nm and 4.1 $\pm$ 0.2 nm, respectively) after attaching deuterated ubiquitin proteins to the diamond surface. Here, twenty NV centers were studied in total. Panels b, d and f show ^{13}C NMR spectra measured on three NV centers (with depths of 4.2 $\pm$ 0.1 nm, 4.7 $\pm$ 0.3 nm and 3.7 $\pm$ 1.1 nm, respectively) after attaching non-deuterated ubiquitin proteins to the diamond surface. Here, ten NV centers were studied in total. The shaded green regions denote the spectral resolution.

The magnetic field for each measurement is indicated. The microwave frequency can be determined by multiplying the magnetic field by the appropriate gyromagnetic ratio (1070.5 Hz/G for ^{13}C and 653.6 Hz/G for ^{2}H). All spectra presented here were acquired using integration times of approximately one to three days.

7.2 Characterization of Ubiquitin Proteins Using Conventional NMR

We verify the deuteration of the proteins by comparing the ^{1}H NMR spectrum of ^{2}H-labeled ubiquitin proteins to that of the unlabelled protein (Figs. S8a and S8b). Here the samples are suspended at 2 mg/ml in 90% H_20, 10% D_20. We use an Agilent DD2 600 MHz spectrometer and implement a Double Pulsed Field Gradient Spin Echo (DPFGSE) pulse sequence to suppress the background solvent signal. The deuterated-Ubiquitin spectrum is dominated by the NMR-active amide-protons in the protein backbone while the vast majority of deuterons are not solvent-accessible and therefore do not contribute to the ^{1}H

spectrum.

8 The Spurious 2/13 Harmonic of ^{1}H

As shown in [34], the spurious 2/13 harmonic of ^{1}H (which is within 0.3% of the ^{2}H Larmor frequency) can be present in XY8-k NMR spectra when coherent evolution during the π-pulses cannot be neglected. In order to rule out the presence of this harmonic, we apply an external calibration signal at frequency 10.312 MHz (simulating a large ^{1}H NMR signal) and measure the NMR spectrum in the vicinity of the 2/13 harmonic (1.587 MHz). We observe that in addition to the 2/13 harmonic, the simulated signal produces additional 4/25 and 4/27 harmonics with amplitude larger than the 2/13 harmonic (Fig. S9). Due to the absence of these additional harmonics in our ^{2}H NMR spectra, we rule out that the observed deuterium signals arise from background hydrogen. We additionally note that the observed deuterium linewidths are a factor of $\sim$10 larger than that measured on the spurious hydrogen harmonic, providing additional verification that our signals cannot be attributed to background hydrogen.

9 NV-based Quadrupolar Spectroscopy of Individual Molecules

9.1 Physical Principles of Single Molecule Quadrupolar Spectroscopy

In this section, we outline the method for determining the structure of a molecule using quadrupolar spectroscopy. As is well-known from conventional Nuclear Quadrupole Resonance (NQR) (*20*), a nuclear spin with $I > 1/2$ possesses an electric quadrupole moment Q. In the absence of a magnetic field, the Hamiltonian of such a spin with $I = 1$ (e.g. ^{2}H

or ^{14}N) is given by

$$H_q = \frac{e^2qQ}{4}\left[3S_{z'}^2 + \eta\left(S_{x'}^2 - S_{y'}^2\right)\right] \tag{19}$$

where e is the electric charge quantum, S_μ are spin vector operators in direction $\vec{\mu}$, and the parameters q and η are determined by the local electric field gradient (EFG) at the position of the nucleus in its principal coordinate system $\{\vec{x'}, \vec{y'}, \vec{z'}\}$ (*35*). The quantities e^2qQ and η are conventionally known as the quadrupole coupling constant (QCC) and the asymmetry parameter (AP), respectively and are typically determined experimentally for each compound of interest. Defining $\bar{Q} = e^2qQ$, the eigenvalues of this Hamiltonian can be computed and are given by

$$E_0 = -\frac{1}{2}\bar{Q}, E_{\pm1} = \frac{(1 \pm \eta)}{4}\bar{Q}, \tag{20}$$

up to a constant shift, with corresponding eigenstates $|m_s = 0\rangle, |\pm\rangle = (|m_s = 1\rangle \pm |m_s = -1\rangle)/\sqrt{2}$. In general, all three transitions between any two of these eigenstates have a non-zero matrix element for a spin vector operator, thereby creating magnetic field noise at the frequencies

$$\nu_\pm = \frac{3 \pm \eta}{4}\bar{Q}, \tag{21}$$

$$\nu_0 = \frac{\eta}{2}\bar{Q}, \tag{22}$$

thus allowing both $\bar{Q}$ and η to be extracted for the zero-field spectrum.

When an external magnetic field is applied, the Zeeman coupling $H_z = -g\mu_B\vec{S}\cdot\vec{B}$ modifies the eigenvalues of the spin states, leading to a change in the magnetic field noise spectrum. We note that this modification is strongly dependent on the orientation of the external magnetic field with respect to the spin axes defined by $\vec{x'}, \vec{y'}$ and $\vec{z'}$. Therefore, by measuring the noise spectrum at various magnetic fields, one can infer the orientation

of the spin relative to the external magnetic field. As an example, in the limit of small magnetic field $B \ll \eta\bar{Q}/\mu_B g$, the second order correction to the spectral peak positions are given by:

$$\Delta\nu_+ = \frac{4(\mu_B g)^2}{\bar{Q}}\left(\frac{B_{z'}^2}{2\eta} + \frac{2B_{x'}^2}{3+\eta} + \frac{B_{y'}^2}{3-\eta}\right) \tag{23}$$

$$\Delta\nu_- = \frac{4(\mu_B g)^2}{\bar{Q}}\left(\frac{-B_{z'}^2}{2\eta} + \frac{B_{x'}^2}{3+\eta} + \frac{2B_{y'}^2}{3-\eta}\right) \tag{24}$$

$$\Delta\nu_0 = \Delta\nu_+ - \Delta\nu_-, \tag{25}$$

from which one can obtain the value of $\sin^2\theta(3-\eta\cos(2\phi))$, where θ and ϕ are polar and azimuthal angles of $\vec{B}$ in the principal coordinate system. Complete information of the orientation can be obtained by varying the orientation of the external magnetic field.

In contrast to conventional NMR spectroscopy with crystallized samples, the position of each spin can also be identified. When the detector is itself a nanoscale object located in close proximity to the target molecule, the amplitude of each spectral line depends sensitively on the position of the corresponding nuclear spin relative to the detector. This spatial dependence arises from the radial and angular dependence of the magnetic dipole interaction of each nuclear spin with the nanoscale probe. This effect is illustrated in Fig. S10a and S10b, where the magnetic noise spectrum of a single spin is computed for different positions (S1 and S2) and orientations (S2 and S3). In general, for given values of the QCC and AP, the 1-dimensional quadrupolar spectrum is a function of $\vec{r}$, $\vec{B}$ and principal coordinates $\hat{x}', \hat{y}', \hat{z}'$. Therefore, measurement of the spectrum in several external magnetic field (amplitudes and orientations) yields information about the molecular structure (Fig S10c), irrespective of the location of the target molecule. This extraction of spatial coordinates of target spins based on magnetic-field dependent spectra is similar to the procedure used in [4], where the positions of several electronic spins were extracted based on their orientation-dependent interaction with a proximal NV

center.

A typical biomolecule (e.g. amino acid, protein) may contain many inequivalent quadrupolar nuclei, each with a different principal coordinate system and each possessing its own characteristic QCC and AP. In a high-field bulk spectrum, containing a macroscopic number of randomly-oriented molecules, these orientation dependent shifts yield a characteristic Pake doublet spectrum (*19*) for each equivalent (possessing the same QCC and AP) nuclear spin (see Fig. 4b, bottom panels). In the limit when only a single molecule contributes to the observed spectrum, however, the Pake doublets break up into potentially resolvable lines, with each nuclear spin contributing three spectral lines. Therefore, the problem of determining the structure of a molecule, assuming that it is fully determined by the positions of the quadrupolar nuclei (as in ^{2}H spectra of deuterated proteins), effectively reduces to finding sets of three spectral peaks corresponding to each nuclear spin and identifying its position and orientation. We note that this task is essentially equivalent to a pattern matching problem since each spin-1 with a given QCC, AP, position and orientation has a well-defined dependence on the external magnetic field (as shown in Fig. S10c and Fig. 4c). We also emphasize that the computational cost of this task is greatly reduced in case there are known constrains on the structure of a molecule (e.g. the sequence of amino acid in a protein). The details of this technique will be described in a forthcoming publication.

9.2 Simulations of Quadrupolar Spectra

We illustrate the physics of quadrupolar spectroscopy by considering the model system deuterated Phenylalanine, one of the essential amino acids that make up proteins.

In order to simulate the ^{2}H quadrupolar spectrum, we model Phenylalanine as an interacting system of deuterons in the C-D, C-D_2 and aromatic groups of the amino acid.

We neglect deuterons in the amine and carboxylic groups, which readily exchange with hydrogen in the environment. We assume typical (*19, 37*) QCC values of 120 kHz, 110 kHz and 130 kHz for deuterons in the C-D, C-D_2 and aromatic groups, respectively. The effects of APs, which tend to be very small for systems of this type (on the order of $\sim$0.05), are neglected (*36*). We assume the quadrupolar axis to be oriented along the C-D bond in all cases. In order to simulate the ^{14}N spectrum, we use the known values of $\bar{Q}$ = 1.354 MHz and $\eta = 0.63$ (*38*). In our simulations the amino acid is fixed on the diamond surface in one of three configurations (Fig 4b - top three panels) and an NV center 4 nm below the (100)-oriented surface is used to probe the variance of the magnetic field fluctuations along its axis. We simulate applying an XY8-1299 sequence, resulting in a mean spectral resolution of $\sim$5 kHz, corresponding to a T_2 of 200 μs. Because of the large quadrupole moment of ^{14}N, the spectral resolution is variable if the number of π-pulses is kept constant during spectrum acquisition. Consequently, if the optimal spectral resolution is to be used in all parts of the spectrum, the number of π-pulses would need to be adjusted dynamically. In our simulations we assume a constant spectral resolution of $\sim$5 kHz. We assume an additional 4 kHz broadening arising from the dipolar coupling of each ^{14}N to its nearest ^{1}H spin.

The change in orientation or conformation of an individual Phenylalanine amino acid, measured by monitoring the amplitude of a single resonance in Fig. 4b, can be detected in approximately $\sim$3 seconds using the techniques outlined in section 5. For this estimate, we assume that the target molecule can deterministically be placed above a 3 nm deep NV center and that the coherence time can be improved by a factor of $\sim$3 beyond what was demonstrated in this work.

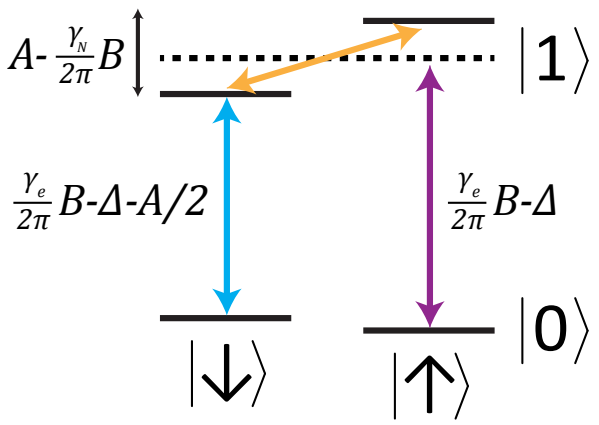


Figure S1: **The level structure of the two-qubit register consisting of a NV center electronic spin and its associated ^{15}N nuclear spin.** The driving fields used for coherent control of the register are indicated. Here $A = 3.05$ MHz is the splitting of the nitrogen hyperfine levels, γ_N is the ^{15}N gyromagnetic ratio and B is the magnitude of the external magnetic field applied along the NV symmetry axis.

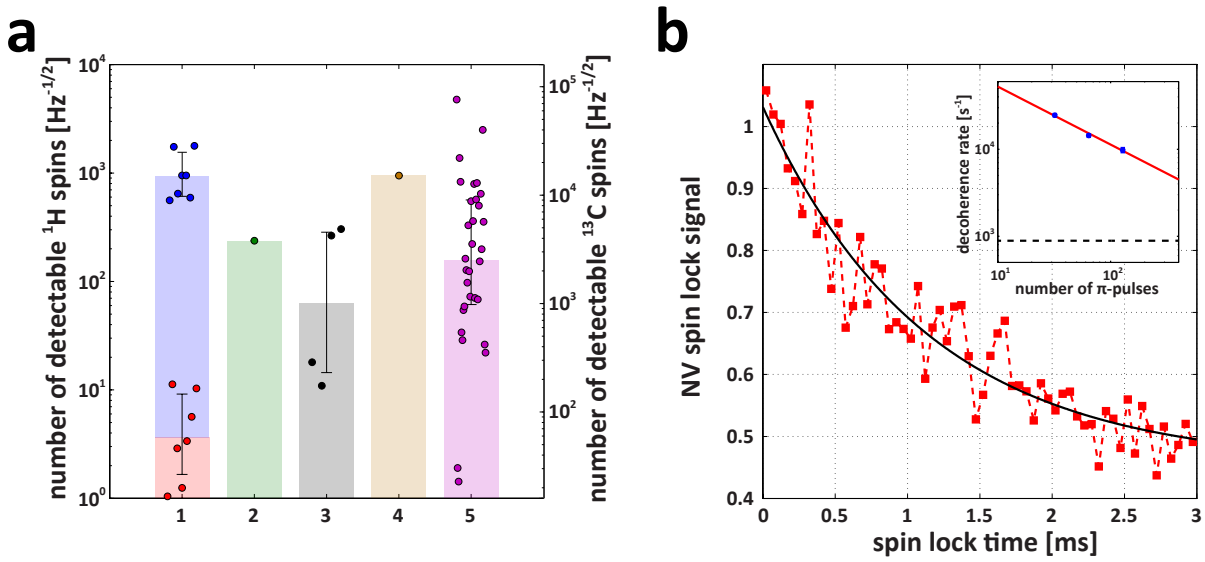


Figure S2: **Minimum detectable number of ^{1}H and ^{13}C spins as measured in our experiments, and compared with previous work reported in the literature.** **a**The bars represent the following: **1)**. Measurements presented in Fig. 2a of the main text before surface treatment and quantum logic-based readout (blue points) and after surface treatment and employing quantum logic-based readout (red points). **2)**. Staudacher et al., Science 339, 561563 (2013), **3)**. Loretz et al., Applied Physics Letters 104, 033102 (2014), **4)**. Myers et al., Physical Review Letters 113, 027602 (2014), **5)**. Romach et al., Physical Review Letters 114, 017601 (2015) with additional NV centers measured by Ulm and Harvard groups on a nominally-identical sample. **b** Measurement of T_1^ρ using spin lock sequence using an NV center with depth 8.3 $\pm$ 1.1 nm. Here an initial $\pi/2$ pulse creates a coherent superposition of the $m_s = 0$ and $m_s = 1$ NV sublevels and a continuous microwave spin lock pulse, with an orthogonal phase, is applied. Subsequently, a second $\pi/2$ pulse converts the signal into a measurable population difference. Here, the spin lock frequency (6 MHz) is held constant while the duration of the spin lock pulse is swept. An exponential fit allows us to extract a $1/T_1^\rho$ rate of 887 $\pm$ 136 s^{-1}. **Inset**, Measurements of XY8-32, XY8-64 and XY8-128 decoherence rates for this NV center (blue points) and fit to $\sim k^{2/3}$ function. The measured value of $1/T_1^\rho$ is indicated by dashed black line.

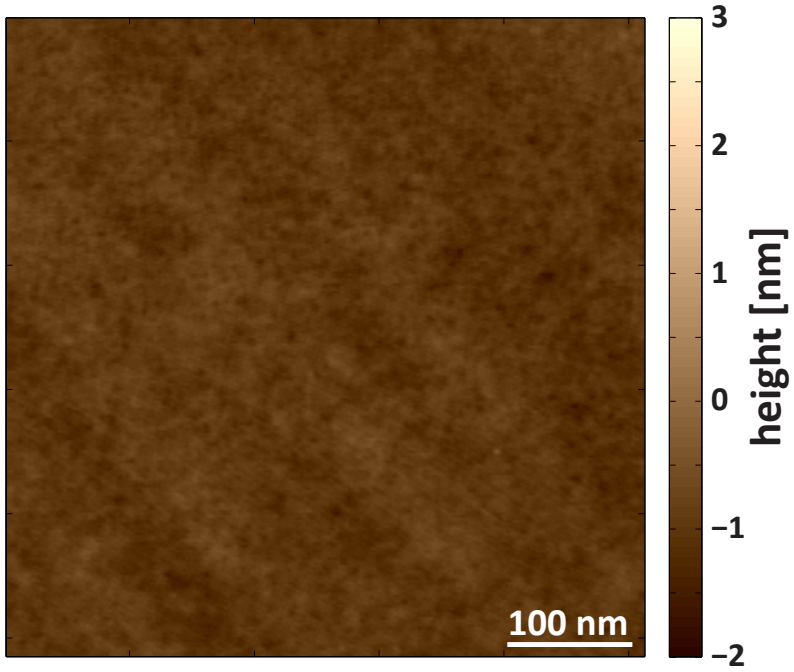


Figure S3: **AFM characterization of clean diamond surface. a**, AFM height image of clean diamond surface acquired using a AC240TS probe. The diamond was cleaned using procedure described in section 1.

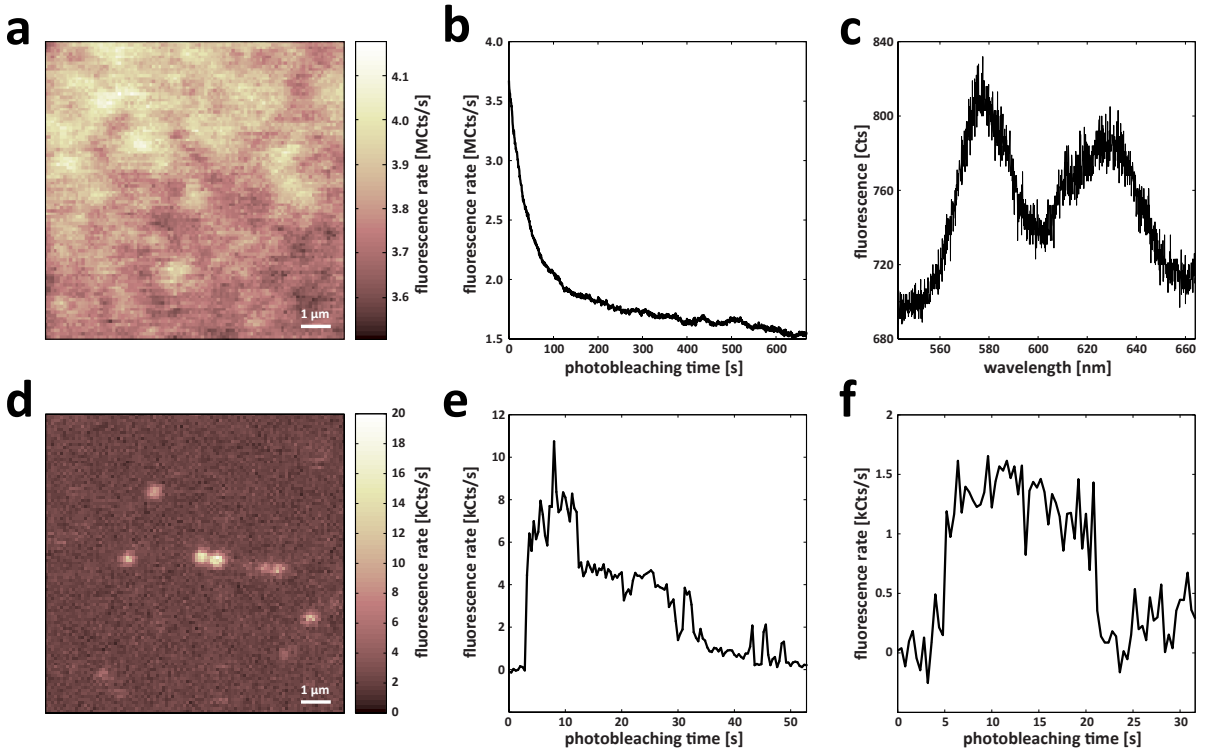


Figure S4: **Protein density calibration using fluorophores.** **a**, High concentration of Cy3+ubiquitin on diamond surface. **b**, Photobleaching timetrace of high density Cy3+ubiquitin on diamond surface. **c**, Fluorescence spectrum of high density Cy3+ubiquitin on diamond surface **d**, Low concentration of Cy3+ubiquitin on diamond surface. Variations in brightness of different spots can largely be explained by an observed variation in single Cy3 dye fluorescence, with a measured mean fluorescence rate of 1.5 kCts/s and a standard deviation of 0.5 kCts/s. **e**, Photobleaching timetrace of a resolved Cy3+ubiquitin spot. **f**, Bare Cy3 dye (no ubiquitin attached) photobleaching step.

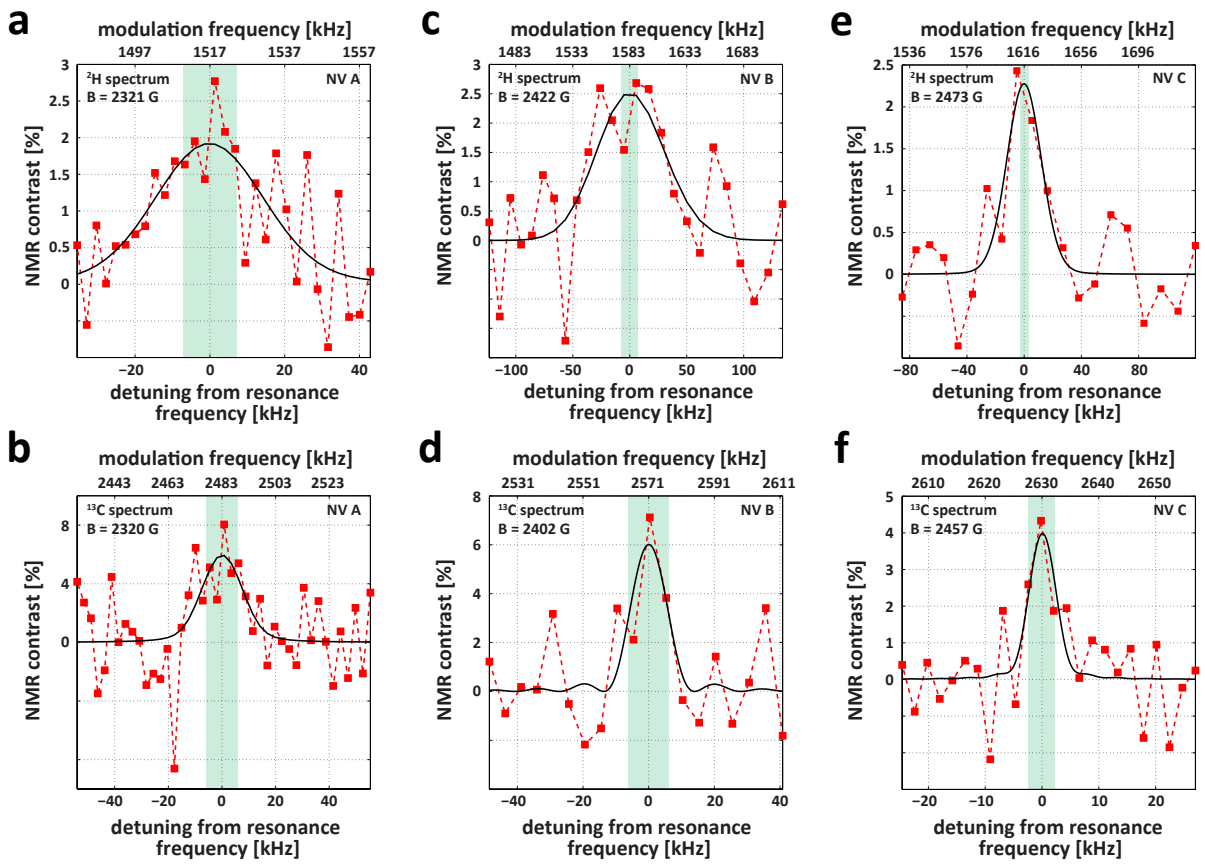


Figure S5: **^{2}H and ^{13}C NMR of deuterated ubiquitin proteins. a,c,e**, ^{2}H NMR spectra of deuterated ubiquitin performed on three NV centers. **b,d,f**, ^{13}C NMR spectra of deuterated ubiquitin performed on the same three NV centers. All spectra are fit with gaussian functions, convolved with the detector filter function. The filter function is determined by the spectral resolution, shown by green shaded regions.

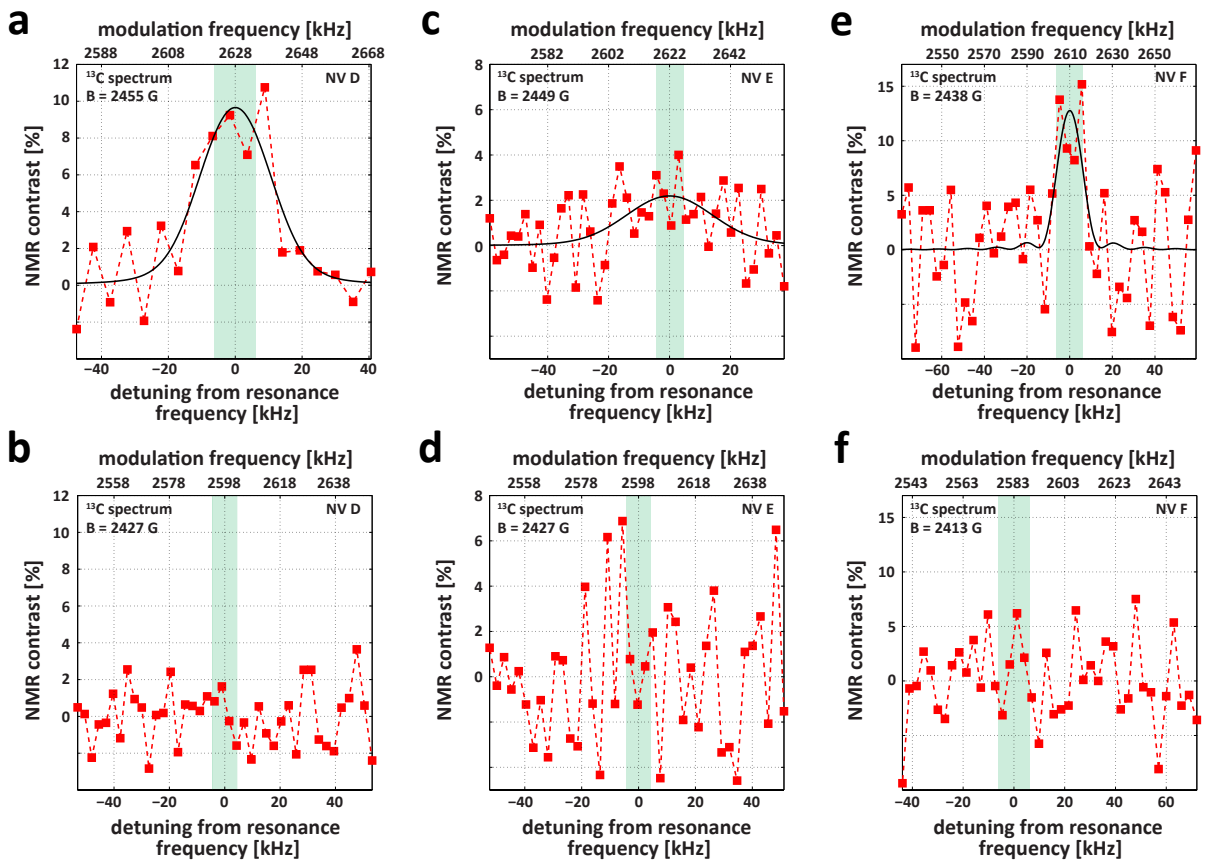


Figure S6: **^{13}C NMR of non-deuterated ubiquitin proteins. a,c,e**, ^{13}C NMR spectra of non-deuterated ubiquitin performed on three NV centers. **b,d,f**, ^{13}C NMR spectra of the same three NV centers after proteins have been removed. All spectra are fit with gaussian functions, convolved with the detector filter function. The filter function is determined by the spectral resolution, shown by green shaded regions.

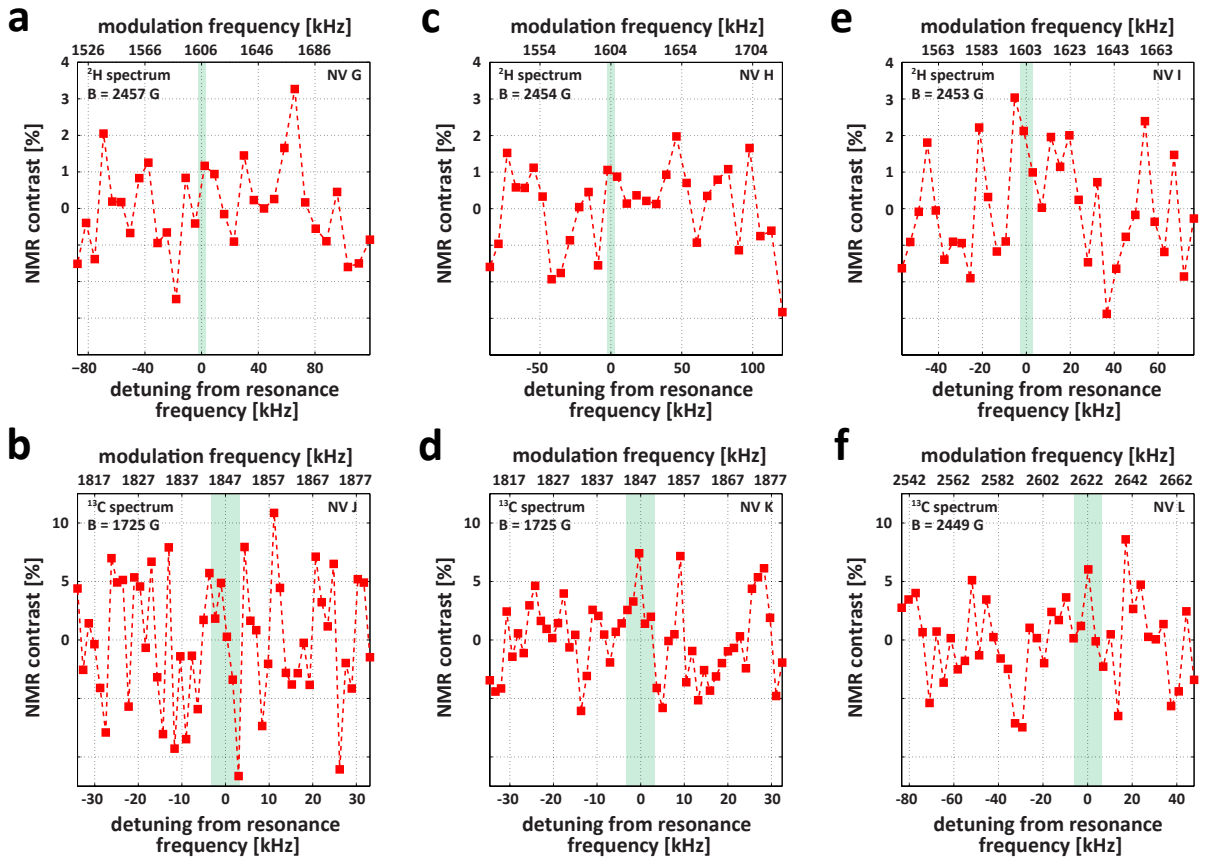


Figure S7: **^{2}H and ^{13}C NMR spectra measured on NV centers with no proximal proteins. a,b,c**, ^{2}H NMR spectra measured on several NV centers after attachment of deuterated ubiquitin. **d,e,f**, ^{13}C NMR spectra measured on several NV centers after attachment of non-deuterated ubiquitin.

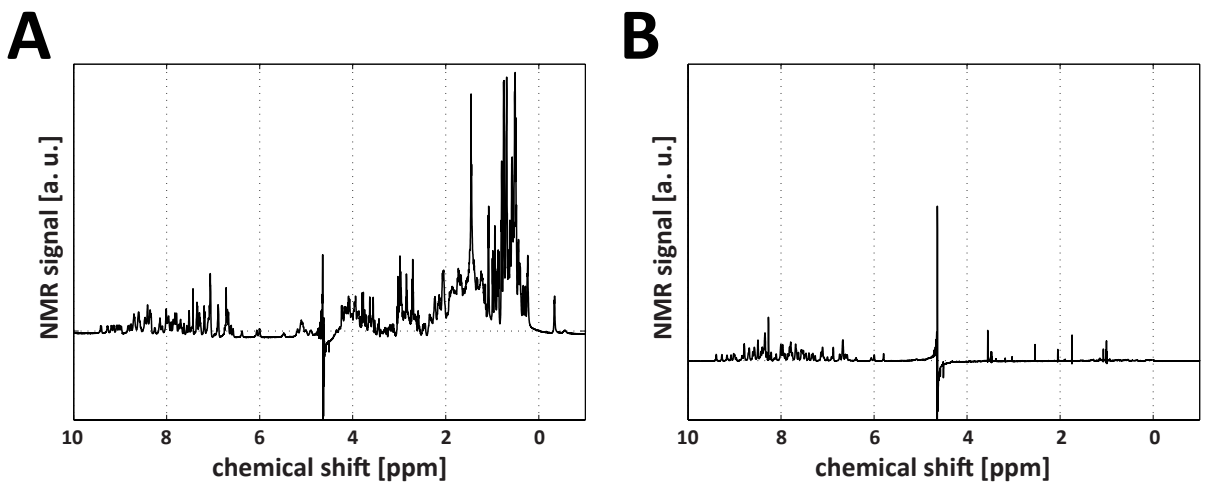


Figure S8: **Conventional NMR spectra of ubiquitin.** **a**, Liquid-state ^{1}H NMR spectrum of unlabelled ubiquitin. Here the Double Pulse Field Gradient Spin Echo (DPFGSE) pulse sequence was used for solvent suppression. **b**, Analogous ^{1}H NMR spectrum of deuterated ubiquitin.

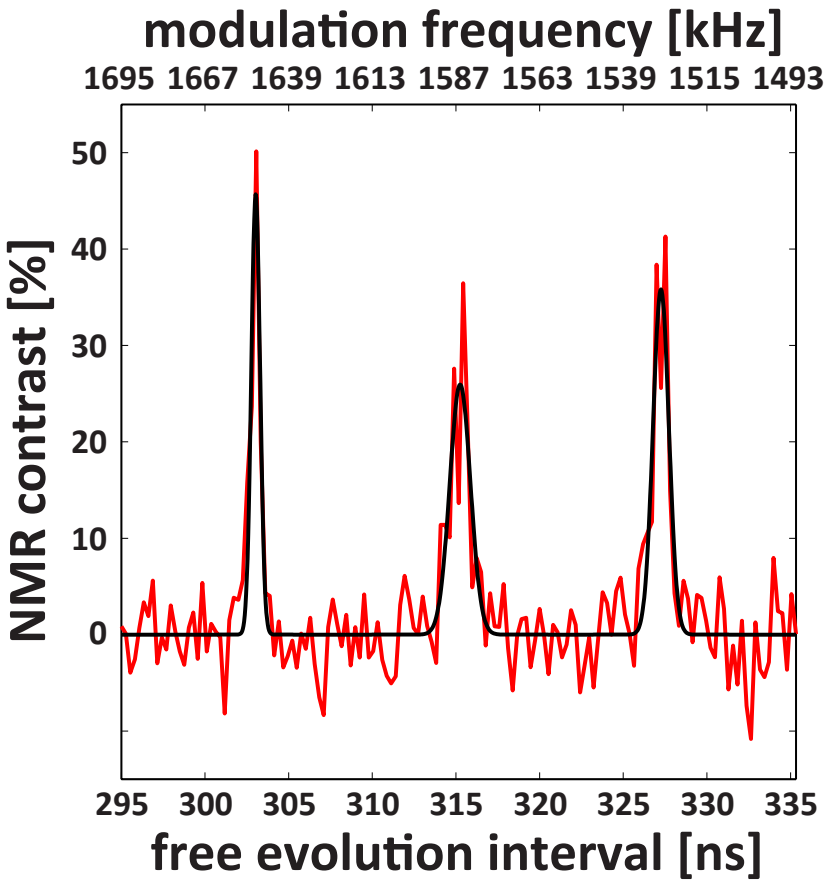


Figure S9: **The spurious harmonics of hydrogen.** Measurement of spurious 4/25, 2/13 and 4/27 harmonics of XY8-k measured using external calibration signal at frequency 10.312 MHz.

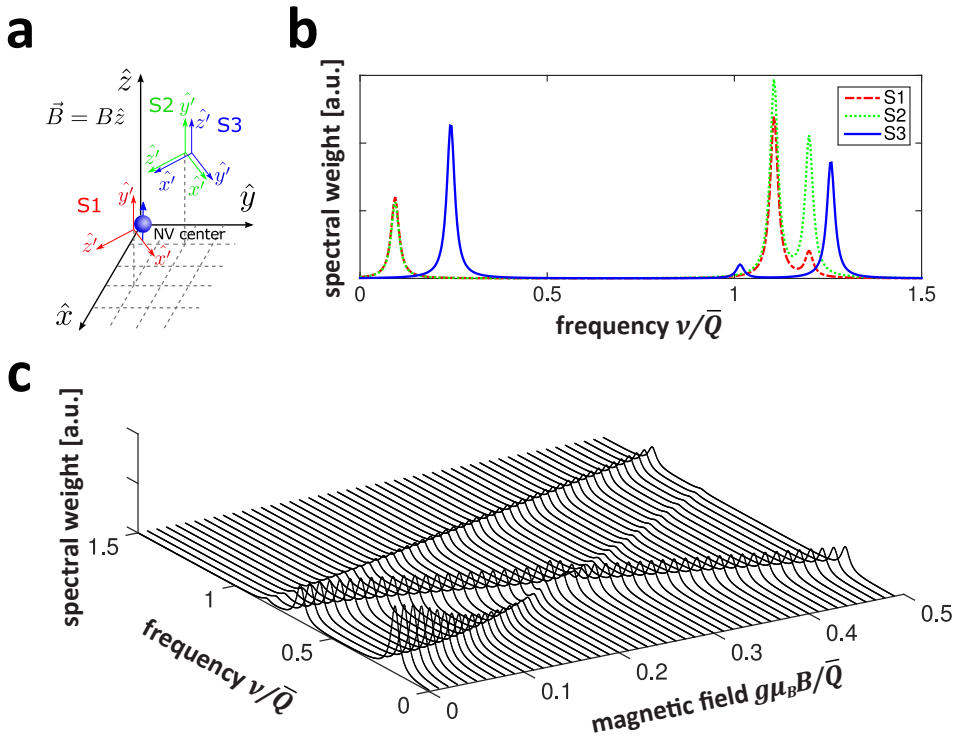


Figure S10: **Principles of quadrupolar spectroscopy with NV centers.** **a**, Various positions and orientations for spins with quadrupolar moments. The axes with $\hat{x}', \hat{y}', \hat{z}'$ denotes the principal axes for each spin's quadrupolar interaction. **b**, Three spectral peaks appear for each spin-1. While the resonance frequencies are determined by the orientation of the principal coordinate system relative to the external magnetic field B (here chosen such that $g\mu_B B = 0.5\bar{Q}$), the weights of the resonances depend on the positions of the spins (S1 and S2). A different orientation at the same position gives a distinct set of spectral peaks (S2 and S3). We assume a value of $\eta = 0.35$ for these simulations. **c**, Magnetic field dependence of the three spectral lines shown in (b), blue curve.

	depth [nm]	$1/T_2$ [kHz]	depth [nm]	$1/T_2$ [kHz]
NV 1	5.3 ± 0.1	53.1 ± 4.6	3.1 ± 0.1	13.0 ± 1.1
NV 2	6.5 ± 0.1	49.9 ± 1.5	5.1 ± 0.2	9.9 ± 1.1
NV 3	5.1 ± 0.1	67.4 ± 0.7	4.8 ± 0.2	5.9 ± 0.4
NV 4	5.0 ± 0.1	97.6 ± 2.8	4.0 ± 0.1	6.9 ± 0.8
NV 5	5.6 ± 0.1	59.2 ± 1.9	5.3 ± 0.1	4.8 ± 0.4
NV 6	5.1 ± 0.1	64.8 ± 1.0	4.9 ± 0.1	7.9 ± 1.1
NV 7	7.3 ± 0.1	33.0 ± 4.8	6.2 ± 0.3	5.0 ± 0.6

Table S1: Experimental measurements of NV depth and XY8-187 decoherence rates $1/T_2$ for several NV centers before (white, columns 1 and 2) and after (grey, columns 3 and 4) oxygen anneal. Errors indicate 68% confidence intervals.

References and Notes

1. P. Glover, S. P. Mansfield, Limits to magnetic resonance microscopy. *Rep. Prog. Phys.* **65**, 1489–1511 (2002). doi:10.1088/0034-4885/65/10/203

2. H. J. Mamin, M. Kim, M. H. Sherwood, C. T. Rettner, K. Ohno, D. D. Awschalom, D. Rugar, Nanoscale nuclear magnetic resonance with a nitrogen-vacancy spin sensor. *Science* **339**, 557–560 (2013). Medline doi:10.1126/science.1231540

3. T. Staudacher, F. Shi, S. Pezzagna, J. Meijer, J. Du, C. A. Meriles, F. Reinhard, J. Wrachtrup, Nuclear magnetic resonance spectroscopy on a (5-nanometer)^3 sample volume. *Science* **339**, 561–563 (2013). Medline doi:10.1126/science.1231675

4. A. O. Sushkov, I. Lovchinsky, N. Chisholm, R. L. Walsworth, H. Park, M. D. Lukin, Magnetic resonance detection of individual proton spins using quantum reporters. *Phys. Rev. Lett.* **113**, 197601 (2014). Medline doi:10.1103/PhysRevLett.113.197601

5. J. M. Taylor, P. Cappellaro, L. Childress, L. Jiang, D. Budker, P. R. Hemmer, A. Yacoby, R. Walsworth, M. D. Lukin, High-sensitivity diamond magnetometer with nanoscale resolution. *Nat. Phys.* **4**, 810–816 (2008). doi:10.1038/nphys1075

6. L. Childress, R. L. Walsworth, M. D. Lukin, Atom-like crystal defects: From quantum computers to biological sensors. *Phys. Today* **67**, 38–43 (2014). doi:10.1063/PT.3.2549

7. S. Kolkowitz, Q. P. Unterreithmeier, S. D. Bennett, M. D. Lukin, Sensing distant nuclear spins with a single electron spin. *Phys. Rev. Lett.* **109**, 137601 (2012). Medline doi:10.1103/PhysRevLett.109.137601

8. Materials, methods and supplementary text are available as supplementary materials on *Science* Online.

9. L. Jiang, J. S. Hodges, J. R. Maze, P. Maurer, J. M. Taylor, D. G. Cory, P. R. Hemmer, R. L. Walsworth, A. Yacoby, A. S. Zibrov, M. D. Lukin, Repetitive readout of a single electronic spin via quantum logic with nuclear spin ancillae. *Science* **326**, 267–272 (2009). Medline

10. P. Neumann, J. Beck, M. Steiner, F. Rempp, H. Fedder, P. R. Hemmer, J. Wrachtrup, F. Jelezko, Single-shot readout of a single nuclear spin. *Science* **329**, 542–544 (2010). Medline doi:10.1126/science.1189075

11. Y. Romach, C. Müller, T. Unden, L. J. Rogers, T. Isoda, K. M. Itoh, M. Markham, A. Stacey, J. Meijer, S. Pezzagna, B. Naydenov, L. P. McGuinness, N. Bar-Gill, F. Jelezko, Spectroscopy of surface-induced noise using shallow spins in diamond. *Phys. Rev. Lett.* **114**, 017601 (2015). Medline doi:10.1103/PhysRevLett.114.017601

12. Y. Chu, N. P. de Leon, B. J. Shields, B. Hausmann, R. Evans, E. Togan, M. J. Burek, M. Markham, A. Stacey, A. S. Zibrov, A. Yacoby, D. J. Twitchen, M. Loncar, H. Park, P. Maletinsky, M. D. Lukin, Coherent optical transitions in implanted nitrogen vacancy centers. *Nano Lett.* **14**, 1982–1986 (2014). Medline doi:10.1021/nl404836p

13. M. Kim, H. J. Mamin, M. H. Sherwood, C. T. Rettner, J. Frommer, D. Rugar, Effect of oxygen plasma and thermal oxidation on shallow nitrogen-vacancy centers in diamond. *Appl. Phys. Lett.* **105**, 042406 (2014). doi:10.1063/1.4891839

14. G. Goldstein, M. Scheid, U. Hammerling, D. H. Schlesinger, H. D. Niall, E. A. Boyse, Isolation of a polypeptide that has lymphocyte-differentiating properties and is probably represented universally in living cells. *Proc. Natl. Acad. Sci. U.S.A.* **72**, 11–15 (1975). Medline doi:10.1073/pnas.72.1.11

15. S. Vijay-Kumar, C. E. Bugg, W. J. Cook, Structure of ubiquitin refined at 1.8 Å resolution. *J. Mol. Biol.* **194**, 531–544 (1987). Medline doi:10.1016/0022-2836(87)90679-6

16. J. C. Sheehan, P. A. Cruickshank, G. L. Boshart, A convenient synthesis of water-soluble carbodiimides. *J. Org. Chem.* **26**, 2525–2528 (1961). doi:10.1021/jo01351a600

17. A. O. Sushkov, N. Chisholm, I. Lovchinsky, M. Kubo, P. K. Lo, S. D. Bennett, D. Hunger, A. Akimov, R. L. Walsworth, H. Park, M. D. Lukin, All-optical sensing of a single-molecule electron spin. *Nano Lett.* **14**, 6443–6448 (2014). Medline doi:10.1021/nl502988n

18. M. Loretz, S. Pezzagna, J. Meijer, C. L. Degen, Nanoscale nuclear magnetic resonance with a 1.9-nm-deep nitrogen-vacancy sensor. *Appl. Phys. Lett.* **104**, 033102 (2014). doi:10.1063/1.4862749

19. D. B. Zax, A. Bielecki, K. W. Zilm, A. Pines, D. P. Weitekamp, Zero field NMR and NQR. *J. Chem. Phys.* **83**, 4877 (1985). doi:10.1063/1.449748

20. T. P. Das, E. L. Hahn, *Nuclear Quadrupole Resonance Spectroscopy* (Academic Press Publishers, New York, 1958).

21. B. J. Shields, Q. P. Unterreithmeier, N. P. de Leon, H. Park, M. D. Lukin, Efficient readout of a single spin state in diamond via spin-to-charge conversion. *Phys. Rev. Lett.* **114**, 136402 (2015). Medline doi:10.1103/PhysRevLett.114.136402

22. P. London, J. Scheuer, J. M. Cai, I. Schwarz, A. Retzker, M. B. Plenio, M. Katagiri, T. Teraji, S. Koizumi, J. Isoya, R. Fischer, L. P. McGuinness, B. Naydenov, F. Jelezko, Detecting and polarizing nuclear spins with double resonance on a single electron spin. *Phys. Rev. Lett.* **111**, 067601 (2013). Medline doi:10.1103/PhysRevLett.111.067601

23. T. Staudacher, N. Raatz, S. Pezzagna, J. Meijer, F. Reinhard, C. A. Meriles, J. Wrachtrup, Probing molecular dynamics at the nanoscale via an individual paramagnetic centre. *Nat. Commun.* **6**, 8527 (2015). doi:10.1038/ncomms9527

24. S. Cavadini, Indirect detection of nitrogen-14 in solid-state NMR spectroscopy. *Prog. Nucl. Magn. Reson. Spectrosc.* **56**, 46–77 (2010). Medline doi:10.1016/j.pnmrs.2009.08.001

25. A. Ajoy, U. Bissbort, M. D. Lukin, R. L. Walsworth, P. Cappellaro, Atomic-scale nuclear spin imaging using quantum-assisted sensors in diamond. *Phys. Rev. X* **5**, 011001 (2015).

26. T. A. Klar, R. Wollhofen, J. Jacak, Sub-Abbe resolution: From STED microscopy to STED lithography. *Phys. Scr.* **2014**, 014049 (2014). doi:10.1088/0031-8949/2014/T162/014049

27. D. Rugar, R. Budakian, H. J. Mamin, B. W. Chui, Single spin detection by magnetic resonance force microscopy. *Nature* **430**, 329–332 (2004). Medline doi:10.1038/nature02658

28. C. L. Degen, M. Poggio, H. J. Mamin, C. T. Rettner, D. Rugar, Nanoscale magnetic resonance imaging. *Proc. Natl. Acad. Sci. U.S.A.* **106**, 1313–1317 (2009). Medline doi:10.1073/pnas.0812068106

29. H. S. Chung, K. McHale, J. M. Louis, W. A. Eaton, Single-molecule fluorescence experiments determine protein folding transition path times. *Science* **335**, 981–984 (2012). Medline doi:10.1126/science.1215768

30. I. A. Yudushkin, A. Schleifenbaum, A. Kinkhabwala, B. G. Neel, C. Schultz, P. I. Bastiaens, Live-cell imaging of enzyme-substrate interaction reveals spatial regulation of PTP1B. *Science* **315**, 115–119 (2007). Medline doi:10.1126/science.1134966

31. Ł. Cywiński, R. M. Lutchyn, C. P. Nave, S. Das Sarma, How to enhance dephasing time in superconducting qubits. *Phys. Rev. B* **77**, 174509 (2008). doi:10.1103/PhysRevB.77.174509

32. L. M. Pham, S. J. DeVience, F. Casola, I. Lovchinsky, A. O. Sushkov, E. Bersin, J. Lee, E. Urbach, P. Cappellaro, H. Park, A. Yacoby, M. Lukin, R. L. Walsworth, NMR technique for determining the depth of shallow nitrogen-vacancy centers in diamond. *Phys. Rev. B* **93**, 045425 (2016). doi:10.1103/PhysRevB.93.045425

33. B. A. Myers, A. Das, M. C. Dartiailh, K. Ohno, D. D. Awschalom, A. C. Bleszynski Jayich, Probing surface noise with depth-calibrated spins in diamond. *Phys. Rev. Lett.* **113**, 027602 (2014). Medline doi:10.1103/PhysRevLett.113.027602

34. M. Loretz, J. M. Boss, T. Rosskopf, H. J. Mamin, D. Rugar, C. L. Degen, Spurious harmonic response of multipulse quantum sensing sequences. *Phys. Rev. X* **5**, 021009 (2015).

35. T. Giavani, H. Bildsøe, J. Skibsted, H. J. Jakobsen, A solid-state ^{14}N magic-angle spinning NMR study of some amino acids. *J. Magn. Reson.* **166**, 262–272 (2004). Medline doi:10.1016/j.jmr.2003.10.023

36. M. J. Hunt, A. L. Mackay, Deuterium and nitrogen pure quadrupole resonance in deuterated amino acids. *J. Magn. Reson.* **15**, 402–414 (1974).

37. P. A. Mirau, *Solid State NMR of Polymers* (iSmithers Rapra Publishing, 2001).

38. D. T. Edmonds, C. P. Summers, ^{14}N pure quadrupole resonance in solid amino acids. *J. Magn. Reson.* **12**, 134–142 (1973).